Calibration of Discrete Element Method Contact Parameters and Development of a Bonded Model for Walnut Cake Flakes

Yuntian Gao,[a] Xiaokang Chen,[a,*] Liping Zhang,[b] Fuliang Huang,[c] Wenya Zhang,[b] Mengxiao Fu,[a] and Yicheng Zhang [a]

Cold-pressed walnut cake flakes, a by-product of walnut processing, have considerable potential for valorization. However, research has focused largely on their biochemical properties, with limited attention to their warped morphology and susceptibility to brittle fracture. These research gaps, together with difficulties in measuring contact and mechanical parameters, hinder the structural design and optimization of crushing equipment. Here, the equivalent coefficient of rolling friction was measured using a modified incline-plane method, and contact parameters for the Hertz-Mindlin (no slip) model were calibrated using response surface methodology, with the angle of repose as the response variable. A meta-particle model incorporating a truss-like force-chain structure was developed and coupled with the Bonding V2 model to identify a set of bonding parameters that reproduced the fracture response. The calibrated normal stiffness per unit area, shear stiffness per unit area, normal strength, and shear strength were 4.91×10^{11} N/m^3, 7.71×10^9 N/m^3, 2.66×10^6 Pa, and 7.04×10^5 Pa, respectively. The relative errors between simulated and measured values were below 5% for angle of repose, fracture force, and fracture displacement. This study provides an analytical method and reference parameters for the design and optimization of equipment for crushing walnut cake flakes.

DOI: 10.15376/biores.22.1.558-584

Keywords: DEM; Response surface methodology; Angle of repose; Bonding V2; Parameter calibration

Contact information: a: School of Mechanical Engineering, Xinjiang University, Urumqi 830017, China; b: Yecheng Walnut Industrialization Development Center, Kashgar 844900, China; c: Xinjiang Shuangxing Agricultural Development Co., Ltd., Kashgar 844900, China;
** Corresponding author: Chenxkxju@163.com*

INTRODUCTION

Walnuts are one of the most widely cultivated nut crops in the world and also serve as an important oilseed resource, offering both high nutritional value and significant economic value (Cao *et al*. 2024). China is a major global producer of walnuts. In Xinjiang, China's primary walnut-producing region, the walnut industry earns substantial profits each year from the sale of high-quality walnut kernels. However, lower-quality or defective walnut kernels are generally used to produce high-value-added products such as walnut oil and walnut pulp beverages. Walnut cake flakes—the flake-like solid residue from the cold pressing of walnut kernels—are generated in large quantities during this processing (Ojeda Amador *et al*. 2018). Meanwhile, Xinjiang has used its saline-alkali land resources to develop specialized livestock farming. The sector continues to expand, but limited local feed supplies necessitate costly procurement from other provinces (Yang *et al*. 2025). Rich

in crude protein, amino acids, and crude fiber, walnut cake flakes have potential as an alternative to conventional feed ingredients such as soybean meal and rapeseed meal (Ma *et al*. 2024; Spréa *et al*. 2026). Crushing and grinding are essential pretreatment steps before the fermentation of walnut cake flakes and directly determine the effectiveness of subsequent fermentation. Excessively coarse particles can reduce fiber degradation efficiency, whereas excessively fine particles can undergo gelatinization and form clumps, inhibiting enzymatic hydrolysis. Producing fine particles of uniform size is therefore a key prerequisite for improving the efficiency of walnut cake flake utilization as feed (Teh *et al*. 2021). However, research on walnut cake flakes has focused on their chemical composition and processing methods, while their mechanical properties remain insufficiently characterized by the design of dedicated processing equipment.

The DEM (discrete element method) is a key simulation approach for designing crushing equipment and analyzing the mechanical behavior of materials. Its ability to reproduce material motion and deformation has led to widespread use in mining and agricultural machinery, including analyses of operating mechanisms and structural optimization (Ning *et al*. 2026). Parameter calibration involves experimentally determining ranges of intrinsic material parameters, contact parameters, and mechanical parameters, then using optimization to identify a parameter set that captures the macroscopic physical properties of the material. This process is an essential prerequisite for DEM simulations, and its accuracy directly affects their reliability (Sun *et al*. 2023; Zhang *et al*. 2026). Depending on the application, agricultural materials can be modeled as rigid or deformable. Rigid-material simulations neglect bending and fracture and generally use the Hertz-Mindlin (no slip) model to describe particle collisions, packing, and motion. Deformable-material simulations account for material deformation and fracture by coupling the Hertz-Mindlin (no slip) contact model with the Bonding V2 model, using bond formation and breakage to represent material deformation and fragmentation (Shi *et al*. 2023). Walnut cake flakes are a brittle by-product of oil extraction with an irregular, warped, flake-like morphology and substantial variation in physical properties among individual pieces. Some contact parameters are difficult to measure, and considerable variability in experimental measurements makes the results difficult to use directly for parameter optimization (Ai *et al*. 2024). For rigid-material simulations, researchers have calibrated contact parameters using the Hertz-Mindlin (no slip) model for ginkgo nuts (Liu *et al*. 2024), sugarcane leaves (Ren *et al*. 2022; Lei *et al*. 2023), peanut (Li *et al*. 2026), cotton stalks (Zhao *et al*. 2023; Zhang *et al*. 2024), walnut kernels (Li *et al*. 2025), and safflower (Li *et al*. 2026). These studies, however, have largely addressed materials with regular shapes, with limited attention to warped, flake-like materials. For deformable-material simulations, researchers have coupled the Hertz-Mindlin (no slip) model with the Bonding V2 model to calibrate models of corncobs (Li *et al*. 2022), wheat straw (Shi *et al*. 2023), soybeans (Gou *et al*. 2026), cottonseeds (Li *et al*. 2024), and rice seedling root mats (Jia *et al*. 2025). However, meta-particle modeling based on particle packing or conventional coordinate calculation methods has substantial limitations for thin, brittle oilseed cakes, particularly in accurately representing load transfer through the thickness.

In this study, the intrinsic material parameters, contact parameters, and the compressive mechanical properties of cold-pressed walnut cake flakes were determined through physical experiments. Discrete element numerical simulation of the repose angle formation process was performed using the Hertz-Mindlin (no slip) model. On this basis, the Bonding V2 model was used for the uniaxial compression simulation of walnut cake flakes. Using the Plackett-Burman design, steepest ascent test, and Box-Behnken design,

contact and bonding parameters were optimized through a combination of these methods, with the angle of repose and compressive mechanical parameters as the respective responses. To address the poor force-chain transmission in the thickness direction arising from the geometric characteristics of thin walnut cake flakes, a meta-particle modeling method incorporating an internal truss-like force-chain structure was proposed to reproduce the warped, flake-like morphology and fracture behavior of walnut cake. Optimal sets of contact and bonding parameters were identified and validated. This study aims to establish a DEM model and calibrate its parameters for cold-pressed walnut cake flakes, providing a reliable analytical method and reference parameters for the structural design and parameter optimization of walnut cake flakes crushing equipment.

EXPERIMENTAL

Materials

The walnut cake flakes used in this study were a by-product of the cold-pressed walnut oil production process, provided by Xinjiang Shuangxing Agricultural Development Co., Ltd. in Yecheng County, Kashgar Prefecture, Xinjiang Uygur Autonomous Region, China. The raw material was Xinxin-2 walnut. After harvesting, the green husks were removed *via* a combined mechanical cutting and washing process. Walnut kernels were then obtained through hard shell cracking and a combined vibration-air separation process. High-pressure water jet washing was applied to the kernels to control the seed coat residue below 2%. Subsequently, X-ray inspection was performed to detect internal worm infestation inside the kernels, and defective kernels were then removed by pneumatic sorting. Finally, screw cold pressing was performed to produce cold-pressed crude walnut oil, with walnut cake flakes as the by-product. The moisture content of the ground walnut cake flakes was measured at 80 °C using a moisture content analyzer (Shanghai Yixin Scientific Instruments Co., Ltd., Shanghai, China) (Zhang *et al*. 2026). The arithmetic mean moisture content across 10 measurements was 6.08%. The walnut cake flakes exhibited a broad particle size distribution, which was determined using round-hole sieves and is presented in Table 1.

Table 1. Particle Size Distribution of Walnut Cake Flakes

Particle Size Range (mm)	Mass Percentage (%)
50 ≥	22.13
[40,50)	13.71
[30,40)	20.68
[20,30)	16.65
[15,20)	7.29
[10,15)	5.56
[5,10)	7.91
[1,5)	4.46
[0,1)	1.61

Determination of Intrinsic Material Parameters

The warped, flake-like morphology and brittle nature of walnut cake flakes make compression testing unsuitable for determining its elastic modulus and Poisson's ratio. These parameters were therefore measured using uniaxial tensile tests. To minimize specimen fracture during clamping and the associated measurement errors, pieces with flat

surfaces were selected and sanded into smooth, thin rectangular specimens using 100-grit sandpaper. Strain gauges configured in a full bridge were bonded to the specimen surfaces to measure the strains required to determine Poisson's ratio. The experimental setup is shown in Fig. 1. Before testing, the width and thickness of each specimen were measured, and the initial gauge length was marked. Each specimen was then centered between the upper and lower tensile grips, which were tightened alternately to prevent damage during clamping. Once the specimen was secured, the universal testing machine was operated at a tensile loading speed of 0.5 mm/min, and loading was stopped after 30 s to avoid specimen fracture. Five tests were performed. Poisson's ratio was calculated from the strain measurements using Eq. 1, and the elastic modulus was calculated from data within the elastic deformation region using Eq. 2,

$$\mu = \left| \frac{\varepsilon_{\text{lat}}}{\varepsilon_{\text{axi}}} \right| \quad (1)$$

$$E = \frac{\sigma}{\varepsilon_{axi}} = \frac{FL_0}{A_0 \Delta L} \quad (2)$$

where μ is Poisson's ratio, ε_{axi} and ε_{lat} are the axial and lateral strains, respectively, and all three quantities are dimensionless. E is the elastic modulus (Pa), σ is the axial stress (Pa), F is the axial tensile force (N), L_0 is the initial gauge length (m), A_0 is the cross-sectional area (m^2), and ΔL is the axial elongation (m). Poisson's ratio ranged from 0.11 to 0.38, and the elastic modulus ranged from 2.3×10^7 to 3.2×10^7 Pa. Density was measured using the water-displacement method, with values ranging from 970 to 1566 kg/m^3 across 10 tests.

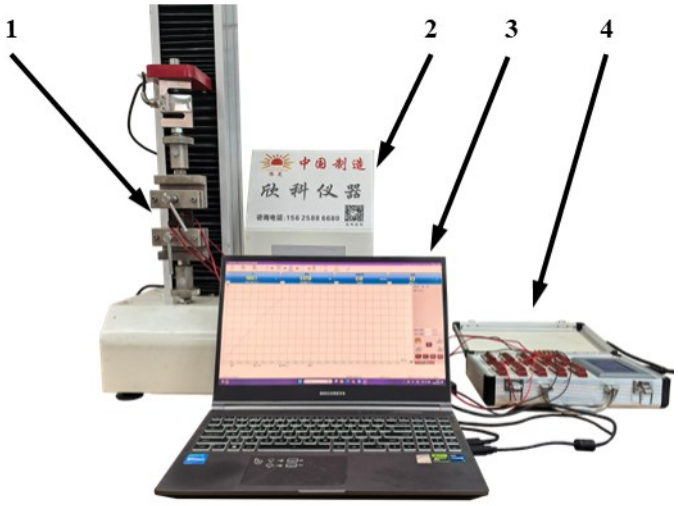


Fig. 1. Experimental setup for elastic modulus and Poisson's ratio uniaxial tensile measurement. 1: Walnut cake flakes; 2: universal testing machine; 3: computer; 4: strain measuring instrument

Determination of Contact Parameters

Determination of the coefficient of restitution

The coefficient of restitution is defined as the ratio of the relative normal separation velocity after a collision to the relative normal approach velocity before the collision at the contact point, as expressed in Eq. 3 (Zhang *et al*. 2025). It was measured using the free-fall method. Before testing, sharp tips on the flake specimens were sanded smoothly to reduce fracture caused by stress concentrations during impact and the resulting measurement

errors. The experimental setup and schematics are shown in Figs. 2 and 3, respectively. A stainless-steel ruler secured in a tensile grip was positioned to the right of the walnut cake flake target plate. A high-speed camera (Daheng Image Vision Co., Ltd., Beijing, China) was placed in front of the test rig and operated at 240 frames/s. Walnut cake flakes are a brittle material with high stiffness and low hardness. During free fall, gravitational potential energy is converted into kinetic energy, which produces an impact when the specimen strikes the target plate. Some specimens fractured on impact, consuming part of the kinetic energy and thereby reducing the measured coefficient of restitution. Accordingly, 15 trials in which no specimen fracture occurred were retained as valid measurements. The measured maximum rebound heights were substituted into Eq. 3,

$$C_{oR} = \frac{v_1}{v'_1} = \frac{\sqrt{2gH}}{\sqrt{2gh}} = \sqrt{\frac{H}{h}} \quad (3)$$

where C_{oR} is the coefficient of restitution (dimensionless), v_1 is the incident velocity before collision (m/s), v'_1 is rebound velocity after collision (m/s), g is gravitational acceleration (m/s^2), H is the drop height before collision (m), and h is the rebound height after collision (m). The coefficients of restitution were 0.223 to 0.455 for walnut cake flake-walnut cake flake contact and 0.228 to 0.437 for walnut cake flake-304 stainless steel contact.

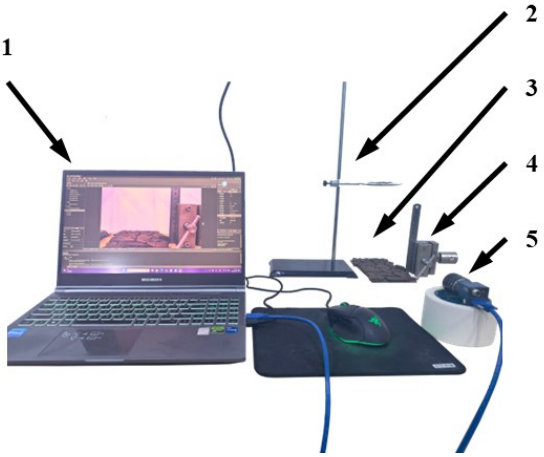


Fig. 2. Experimental setup for coefficient of restitution measurement. 1: Computer; 2: metal support; 3: specimen contact plane; 4: steel ruler; 5: high-speed camera

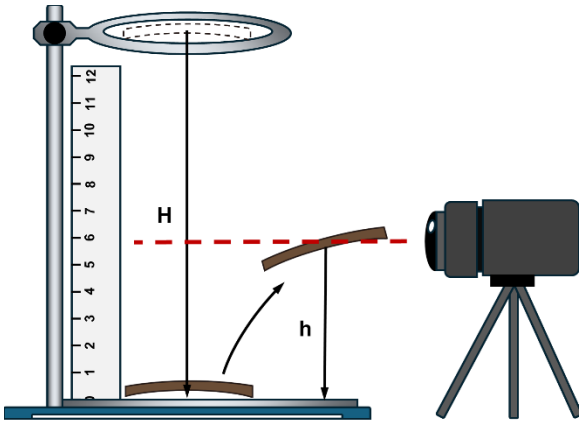


Fig. 3. Principles of tests for determining the coefficient of restitution

Determination of the coefficient of static friction

The coefficient of static friction is the ratio of the frictional force to the normal force at the onset of relative motion between two contacting materials. It was measured using the incline-plane method. The experimental setup and schematic are shown in Figs. 4 and 5, respectively. A digital inclinometer was first calibrated on a level tabletop. A walnut cake flake specimen was then positioned at a gap in the walnut cake flake contact plane. The inclined plane was raised slowly at a constant rate until the specimen exhibited noticeable rocking or slight sliding relative to the contact plane. The inclination angle was recorded using the digital inclinometer after the specimen had come to rest. Fifteen tests were performed, and the measured angles were substituted into Eq. 4,

$$C_{oSF} = \frac{F_f}{F_N} = \frac{mg\sin\alpha}{mg\cos\alpha} = \tan\alpha \quad (4)$$

where C_{oSF} is the static friction coefficient, which is dimensionless, F_f is the frictional force (N), F_N is the normal contact force (N), m is the mass of the walnut cake flake (kg), g is gravitational acceleration (m/s^2), and α is the sliding angle (°). The resulting coefficients of static friction ranged from 0.217 to 0.385 for walnut cake flake-walnut cake flake contact and from 0.166 to 0.24 for walnut cake flake-304 stainless steel contact.

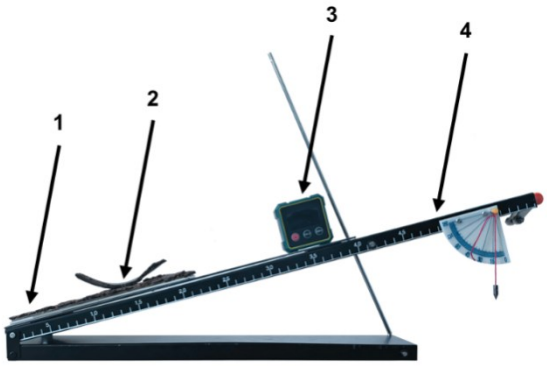


Fig. 4. Experimental setup for static friction coefficient measurement. 1: Specimen contact plane; 2: walnut cake flake; 3: inclinometer; 4: inclined-plane track

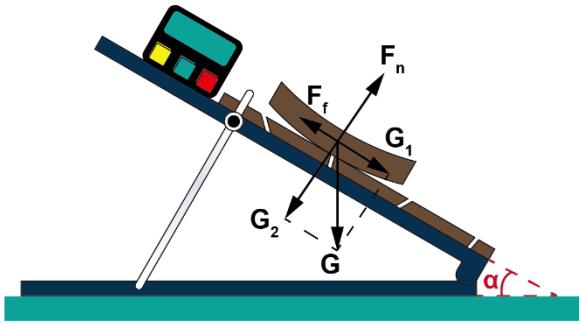


Fig. 5. Schematic diagram of static friction coefficient measurement test by inclined-plane method

Determination of the equivalent coefficient of rolling friction

The coefficient of rolling friction is an equivalent coefficient describing resistance to relative rolling between two contacting bodies. The flake-like morphology of walnut cake flakes makes this coefficient difficult to measure using the conventional incline-plane

method. To address this limitation, a modified incline-plane method using an equivalent roller was developed. A polylactic acid (PLA) cylinder, 30 mm in height and 5 mm in radius, was fabricated using a 3D printer (Creality 3D Technology Co., Ltd., Shenzhen, China). Its surface was uniformly coated with ethyl cyanoacrylate adhesive, and the cylinder was embedded in ground walnut cake powder and held under pressure for 2 h. Loosely adhering particles were then gently removed with a soft brush to obtain a walnut cake-coated roller specimen. The experimental setup and schematic of the modified incline-plane method are shown in Figs. 6 and 7, respectively. A mark was made on the walnut cake flake contact plane on the incline, 100 mm from its lower edge, and the leading edge of the roller was aligned with the mark. With the inclination angle held constant, the distance traveled by the roller on the horizontal reference plate was recorded. Fifteen tests were performed. Equivalent coefficients of rolling friction were calculated using Eq. 5.

$$C_{oRF} = \frac{X \sin \alpha}{X \cos \alpha + L} \tag{5}$$

The values ranged from 0.128 to 0.143 for walnut cake flake-walnut cake flake contact and from 0.062 to 0.091 for walnut cake roller-steel contact. The values for walnut cake flake-walnut cake flake contact were notably higher than those for conventional non-cohesive materials. This difference was attributed to the numerous pronounced gaps in the walnut cake flake contact plane: as the roller entered these gaps, minor collisions between its lower surface and the gap edges dissipated kinetic energy. Drawing on studies of walnut kernels and related oilseed materials, together with the experimental results, a range of 0.05 to 0.143 was selected for the coefficient of rolling friction for walnut cake-walnut cake contact (Li *et al*. 2025).

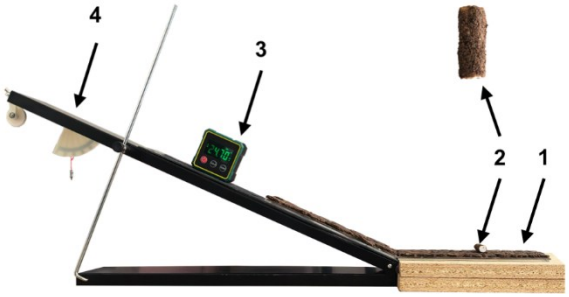


Fig. 6. Experimental setup for coefficient of rolling friction measurement. 1: Specimen contact plane; 2: walnut cake-coated roller; 3: inclinometer; 4: inclined-plane track

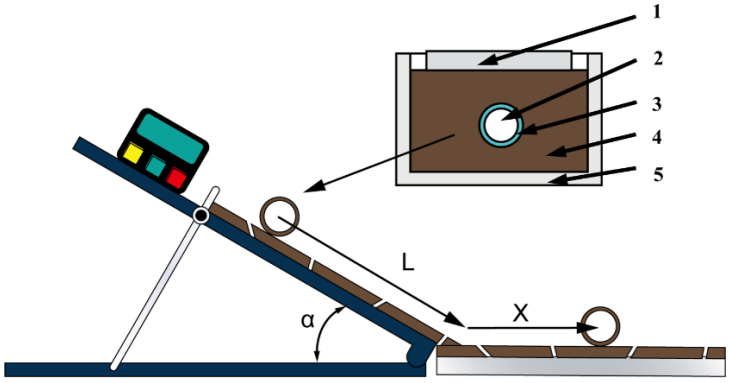


Fig. 7. Principle of the coefficient of rolling friction test. 1: Walnut cake compact; 2: polylactic acid cylinder; 3: adhesive; 4: walnut cake powder; 5: container

Determination of the Physical Angle of Repose

The AoR (Angle of Repose) of walnut cake flakes was measured using the cylinder-lifting method. Preliminary tests showed that piles formed from larger pieces contained large internal voids and exhibited considerable variation in the angle of repose. By contrast, the 15 to 20 mm size fraction produced compact, stable piles with markedly smaller voids. The experimental setup is shown in Fig. 8. A bottomless stainless steel cylinder, 100 mm in diameter, 200 mm in height, and 4 mm in wall thickness, was secured with nano-adhesive between the lower supports of a three-point bending fixture. This assembly was attached to the upper part of a universal testing machine. A square stainless steel base plate, 300 mm on each side and 4 mm thick, was placed on the lower compression platen. The cylinder was filled with 400 g of walnut cake flakes in the 15 to 20 mm size fraction and lifted vertically at 8 mm/s. As the cylinder was raised, the particles lost lateral confinement and moved downward under gravity, with friction between neighboring flakes influencing their motion, until a compact pile formed.

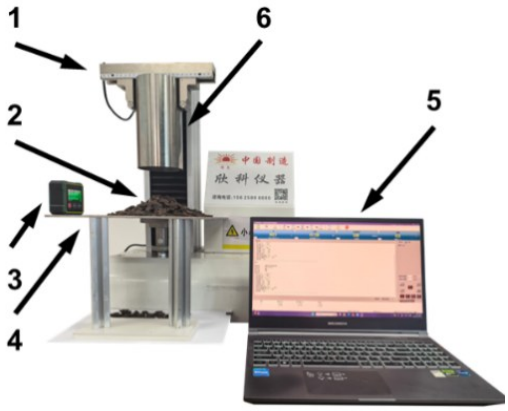


Fig. 8. Experimental setup for angle of repose measurement of walnut cake flakes. 1: Universal testing machine; 2: walnut cake flakes; 3: inclinometer; 4: stainless steel substrate; 5: computer; 6: bottomless stainless steel cylinder

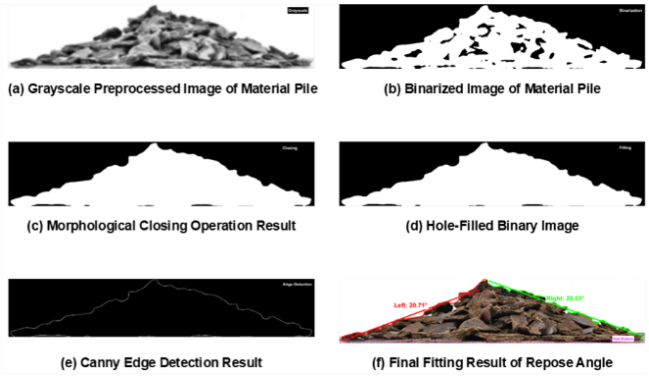


Fig. 9. Fitting the edges of the angle of repose of the walnut cake flakes

Five tests were performed. The resulting pile images were cropped and their backgrounds cleaned using Photoshop (Adobe Inc., CA, USA) to remove visual interference. The images were then processed in MATLAB through grayscale conversion, Gaussian smoothing, and binarization, followed by morphological closing, hole filling, and Canny edge detection to extract the pile contours. To minimize the influence of loose particles at the base on the fitted angle of repose, the bottom 5% of the image height was excluded from fitting. To account for pile asymmetry, the left and right slopes were fitted separately, and the two resulting angles were averaged for each test. The fitted profiles are shown in Fig. 9. The measured angle of repose ranged from 20.04° to 22.04°, with a mean of 21.08°.

Determination of Compressive Mechanical Properties

The compression test setup is shown in Fig. 10. Walnut cake flakes in the 40 to 50 mm size fraction were selected because they retained an intact morphology and exhibited characteristic warpage, making them suitable for investigating fracture behavior under

uniaxial compression. Each specimen was placed on the lower platen in an arched orientation. The upper platen was slowly lowered to a position close to, but not in contact with, the specimen, after which uniaxial compression was performed at 5 mm/min. Selected results from the uniaxial compression tests on intact walnut cake flake specimens are shown in Fig. 11. Ten tests were performed, yielding fracture forces (F_f) of 34.2 to 59.4 N and fracture displacements (D_f) of 1.24 to 2.62 mm. The test results were ranked primarily by F_f, and selected complete force-displacement curves with F_f close to the median were used as experimental references for subsequent calibration of the bonding parameters.

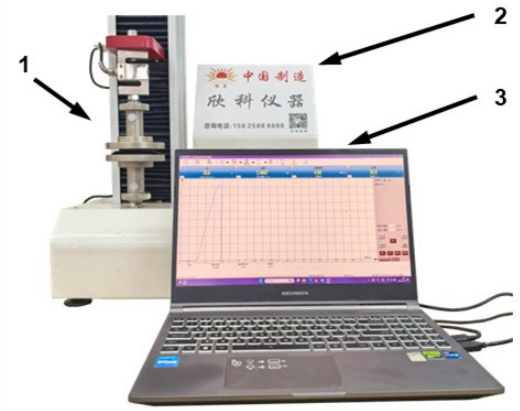


Fig. 10. Experimental setup for uniaxial compression test of a walnut cake flake. 1: Walnut cake flake; 2: universal testing machine; 3: computer

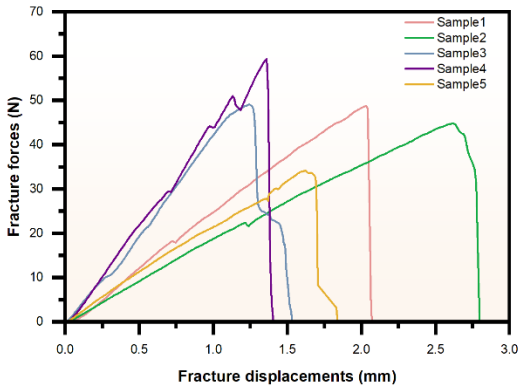


Fig. 11. Uniaxial compression force-displacement curve of walnut cake flake

RESULTS AND DISCUSSION

Calibration of Walnut Cake Flake Contact Parameters

Discrete element model development and simulation setup

The morphology and dimensions of the walnut cake flakes in the 400 g sample used for the cylinder-lifting test were characterized. Based on their appearance, the pieces were classified as long, medium, or small flakes, accounting for 18%, 65%, and 17% of the total number of pieces, respectively (Fig. 12). The geometries of walnut cake flake specimens from these three categories were captured using a handheld 3D scanner (SCANTECH Co., Ltd., Zhejiang, China). The scanned geometries were saved in STL format and imported into EDEM 2024 (DEM Solutions Ltd., Edinburgh, United Kingdom), where particle packing was performed using the Bulk Material function. Three-dimensional models of the stainless steel cylinder and base plate, matching those used in the physical experiment, were created in SolidWorks (Dassault Systèmes SolidWorks Corporation, Massachusetts, USA) and imported into EDEM in STL format. Gravity was directed along the cylinder axis toward the base plate. A particle factory was defined within the cylinder to generate 400 g of walnut cake flakes, matching the mass used in the physical experiment. Once the particle bed had stabilized, the cylinder was lifted at a constant speed of 8 mm/s. The time step was set to 20% of the Rayleigh time step. The simulation was stopped once all walnut cake flakes had exited the cylinder and formed a stable pile on the base plate (Fig. 13). An image of the simulated pile was exported in the post-processing interface. After

background removal in Photoshop, the angle of repose was determined in MATLAB using the same image-processing procedure as for the physical experiments.

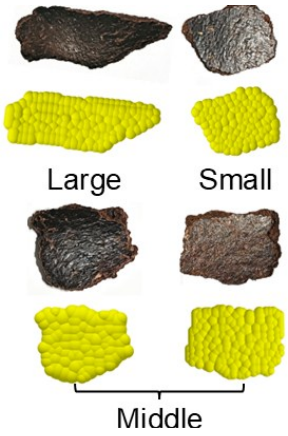


Fig. 12. DEM models for different types of walnut cake flakes

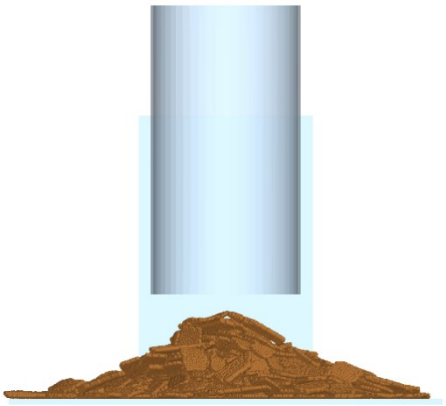


Fig. 13. Simulation tests of the cylinder lifting method

Plackett-Burman test of contact parameters

A Plackett-Burman design was developed in Design-Expert 13 with nine experimental factors and two dummy factors. The design comprised 12 screening runs and five center-point runs, giving 17 runs in total. The experimental factors included the intrinsic material parameters of walnut cake flakes and the contact parameters for walnut cake flake-walnut cake flake and walnut cake flake-stainless steel interactions. The simulated angle of repose obtained using the cylinder-lifting method was used as the response to identify significant factors. Because the selected design provided 11 factor columns, the two columns not assigned to experimental factors were designated as dummy factors, V_0 and V_1, to estimate experimental error without changing the simulation inputs. The factor settings are listed in Table 2. Each simulation run was performed three times, and the mean angle of repose was used as the response.

Table 2. Plackett-Burman Test Parameters

Symbol	Parameters	Level	
		Low(-1)	High(1)
X_0	Density	970	1566
X_1	Poisson's Ratio	0.110	0.380
X_2	Elastic Modulus	2.3×10^7	3.2×10^7
X_3	Coefficient of Static Friction between Walnut Cake Flakes	0.217	0.385
X_4	Coefficient of Rolling Friction between Walnut Cake Flakes	0.050	0.143
X_5	Coefficient of Restitution between Walnut Cake Flakes	0.223	0.455
X_6	Coefficient of Static Friction of Walnut Cake Flakes-Stainless Steel	0.166	0.240
X_7	Coefficient of Rolling Friction of Walnut Cake Flakes-Stainless Steel	0.062	0.091
X_8	Coefficient of Restitution of Walnut Cake Flakes-Stainless Steel	0.228	0.437
V_0, V_1	Dummy Factor	-1	1

The Plackett-Burman design and simulation results are presented in Table 3, and the analysis of variance is summarized in Table 4. The model was statistically significant (P = 0.0004). The dummy factors V_0 and V_1 were not significant, suggesting limited experimental error. Three factors significantly affected the simulated angle of repose: the coefficient of static friction for walnut cake flakes-walnut cake flakes contact X_3, the coefficient of restitution for walnut cake flakes-walnut cake flakes contact X_5, and the coefficient of static friction for walnut cake flakes-stainless steel contact X_6, all with P < 0.05. X_3 was highly significant and dominated pile formation in the cylinder-lifting test.

Table 3. Plackett-Burman Design and Results

No.	X_0	X_1	X_2	X_3	X_4	X_5	X_6	X_7	X_8	V_0	V_1	AoR (°)
1	-1	1	1	-1	1	1	1	-1	-1	-1	1	21.09
2	-1	1	-1	1	1	-1	1	1	1	-1	-1	33.80
3	-1	-1	-1	1	-1	1	1	-1	1	1	1	28.10
4	1	-1	1	1	-1	1	1	1	-1	-1	-1	30.00
5	1	-1	1	1	1	-1	-1	-1	1	-1	1	30.41
6	0	0	0	0	0	0	0	0	0	0	0	26.54
7	1	1	1	-1	-1	-1	1	-1	1	1	-1	20.76
8	1	-1	-1	-1	1	-1	1	1	-1	1	1	23.61
9	0	0	0	0	0	0	0	0	0	0	0	24.63
10	1	1	-1	-1	-1	1	-1	1	1	-1	1	19.73
11	-1	1	1	1	-1	-1	-1	1	-1	1	1	30.24
12	-1	-1	1	-1	1	1	-1	1	1	1	-1	18.88
13	0	0	0	0	0	0	0	0	0	0	0	25.14
14	0	0	0	0	0	0	0	0	0	0	0	26.37
15	-1	-1	-1	-1	-1	-1	-1	-1	-1	-1	-1	18.96
16	1	1	-1	1	1	1	-1	-1	-1	1	-1	27.90
17	0	0	0	0	0	0	0	0	0	0	0	22.69

The remaining six factors had smaller effects and were not statistically significant. Accordingly, X_3, X_5, and X_6 were selected for the steepest ascent test, while the remaining factors were fixed at their coded zero levels: X_0 = 1268 kg/m^3, X_1 = 0.245, X_2 = 2.75 × 10^7 Pa, X_4 = 0.0965, X_7 = 0.0765, and X_8 = 0.333.

Table 4. Significance Analysis of Parameters in the Plackett-Burman Test

Parameter	Effect	Sum of squares	Contribution rate (%)	*F* Values	*P* Values
Model	-	310.77	-	19.72	0.0004**
X_0	0.223	0.1496	0.05	0.0855	0.7785
X_1	0.593	1.06	0.32	0.6032	0.4628
X_2	-0.120	0.0432	0.01	0.0247	0.8796
X_3	9.570	274.75	84.52	156.91	< 0.0001**
X_4	1.317	5.20	1.6	2.97	0.1285
X_5	-2.013	12.16	3.74	6.94	0.0337*
X_6	1.873	10.53	3.24	6.01	0.0440*
X_7	1.507	6.81	2.10	3.89	0.0892
X_8	-0.021	0.0013	0.0004	0.0007	0.9792
Note: ** indicates extremely significant impact (P < 0.01), * indicates significant impact (0.01 < P < 0.05), same below. R^2 = 0.9621, R^2_{adj} = 0.9133, CV = 5.25%, Adeq Precision = 14.6278					

Multiple regression analysis was performed to relate the angle of repose to the coded factor values, yielding Eq. 6:

$$Y = 25.23 + 0.1117X_0 + 0.2967X_1 - 0.0600X_2 + 4.79X_3 + 0.6583X_4 - 1.01X_5 + 0.9367X_6 + 0.7533X_7 - 0.0103X_8 \quad (6)$$

Steepest ascent test of contact parameters

A steepest ascent test was conducted on the three significant factors identified by the Plackett-Burman design to refine their optimal parameter ranges. According to Eq. 6, the coefficients of static friction between walnut cake flakes contact X_3 and walnut cake flakes-steel contact X_6 have positive effects on the angle of repose, whereas the coefficient of restitution for walnut cake flakes-walnut cake contact X_5 has a negative effect. Increasing X_3 and X_6 while decreasing X_5 therefore produces a monotonic increase in the angle of repose predicted by Eq. 6, rather than an increase followed by a decrease. The parameter ranges were thus evaluated using the relative error between the simulated angle of repose and the experimental mean of 21.08°. The steepest ascent design and results are presented in Table 5. Along the tested path, the relative error initially decreased and then increased, reaching its minimum in Run 2.

Table 5. Design and Results of the Steepest Ascent Test for Contact Parameters

No.	X_3	X_5	X_6	AoR (°)	Relative Error (%)
1	0.217	0.455	0.166	18.42	12.62
2	0.251	0.409	0.181	22.36	6.07
3	0.284	0.362	0.196	25.47	20.83
4	0.318	0.316	0.210	28.31	34.30
5	0.351	0.269	0.225	30.74	45.82
6	0.385	0.223	0.24	37.88	79.70

Box-Behnken experiment of contact parameters

Based on the steepest ascent results, a Box-Behnken design was developed using the parameter settings in Run 2 as the center levels and those in Runs 1 and 3 as the endpoints of the factor ranges. The design was used to investigate the effects of the three significant factors and their interactions on the angle of repose of walnut cake flakes. Seventeen cylinder-lifting simulations, including five center-point runs, were conducted, with the simulated angle of repose as the response. Each run was performed three times, and the mean value was used for analysis. The design and results are presented in Table 6. Multiple regression analysis was used to establish a quadratic regression equation relating to the angle of repose to the three significant factors, as expressed in Eq. 7:

$$Y = 22.88 + 2.32X_3 - 0.8780X_5 + 0.4262X_6 + 1.0800X_3X_5 + 0.1940X_3X_6 - 0.2625X_5X_6 + 0.1870X_3^2 - 0.5047X_5^2 - 0.3477X_6^2 \quad (7)$$

The ANOVA results for the quadratic regression model are presented in Table 7. The model was highly significant. The coefficient of static friction for walnut cake flakes-walnut cake flakes contact X_3, the coefficient of restitution for walnut cake flakes-walnut cake flakes contact X_5, and their interaction X_3X_5 had highly significant effects on the response. The coefficient of static friction for walnut cake flakes-steel contact X_6 also had a significant effect. The remaining terms, X_3X_6, X_5X_6, X_3^2, X_5^2, and X_6^2, were not significant. The lack of fit was not significant. The coefficient of determination R^2 and adjusted

coefficient of determination adjusted R^2 were 0.9743 and 0.9414, respectively, and the adequate precision was 20.6603. These results indicated a good fit to the simulation data.

Table 6. Box-Behnken Experimental Design and Results

No.	X_3	X_5	X_6	AoR (°)
1	0.217	0.409	0.166	19.93
2	0.251	0.409	0.181	23.07
3	0.251	0.409	0.181	22.74
4	0.284	0.455	0.181	24.95
5	0.251	0.362	0.166	22.32
6	0.284	0.409	0.196	25.89
7	0.251	0.362	0.196	23.24
8	0.251	0.455	0.196	21.28
9	0.284	0.409	0.166	24.18
10	0.217	0.362	0.181	22.33
11	0.284	0.362	0.181	24.85
12	0.251	0.409	0.181	22.23
13	0.217	0.455	0.181	18.13
14	0.217	0.409	0.196	20.85
15	0.251	0.409	0.181	23.53
16	0.251	0.409	0.181	22.97
17	0.251	0.455	0.166	21.42

Table 7. Analysis of ANOVA for Angle of Repose

Parameter	Sum of squares	Freedom	Mean Square	*F* Values	*P* Values
Model	57.63	9	6.40	29.54	< 0.0001**
X_3	43.17	1	43.17	199.14	< 0.0001**
X_5	6.17	1	6.17	28.45	0.0011**
X_6	1.45	1	1.45	6.70	0.0360*
X_3X_5	4.64	1	4.64	21.41	0.0024**
X_3X_6	0.1506	1	0.1506	0.6946	0.4321
X_5X_6	0.2756	1	0.2756	1.27	0.2967
X_3^2	0.1472	1	0.1472	0.6792	0.4370
X_5^2	1.07	1	1.07	4.95	0.0615
X_6^2	0.5089	1	0.5089	2.35	0.1693
Residual	1.52	7	0.2168		
Lack of Fit	0.6125	3	0.2042	0.9025	0.5141
Pure Error	0.9049	4	0.2262		
Summation	59.15	16			
R^2 = 0.9743; Adj R^2 = 0.9414 CV = 2.06%; Adeq Precision = 20.6603					

As shown in Fig. 14, at a fixed coefficient of static friction for walnut cake flakes-steel contact X_6, the angle of repose increases slightly with the coefficient of static friction between walnut cake flakes contact X_3 but decreases markedly with the corresponding coefficient of restitution X_5. The simulated cylinder-lifting process can be divided into three stages according to the motion of the walnut cake flakes: an essentially stationary stage, a rapid collapse stage, and a concentrated discharge stage (Fig. 15). During the essentially stationary stage, the cylinder rises at a constant speed while most flakes remain stationary on the stainless steel base plate, with sliding confined to the pile edges. The coefficient of static friction for walnut cake flakes-steel contact X_6 dominates this stage. Once the

cylinder reaches a certain height, flakes near the base plate collapse abruptly, initiating the rapid collapse stage and forming the initial pile base. All three significant factors play major roles during this stage. During the subsequent concentrated discharge stage, flakes fall successively as the cylinder rises and collides with those already deposited below. Repeated collisions progressively reduce the rebound height, and relative sliding between flakes then occurs until a stable pile forms. During this stage, normal contact forces between the falling flakes and the cylinder or stainless steel plate are small, so these contacts no longer dominate the process. Instead, interactions between walnut cake flakes govern their motion, accounting for the significant effects of X_3, X_5, and their interaction, X_3X_5.

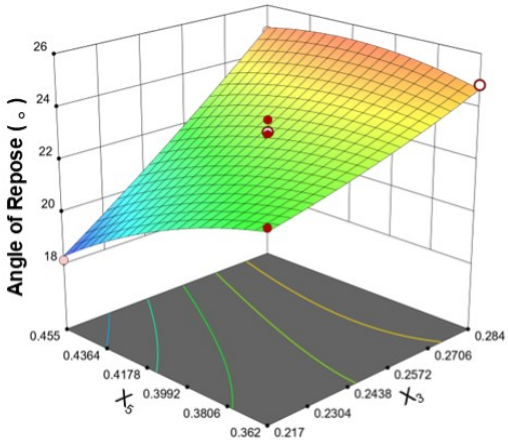


Fig. 14. Response surface for the significant interaction between walnut cake flakes and angle of repose

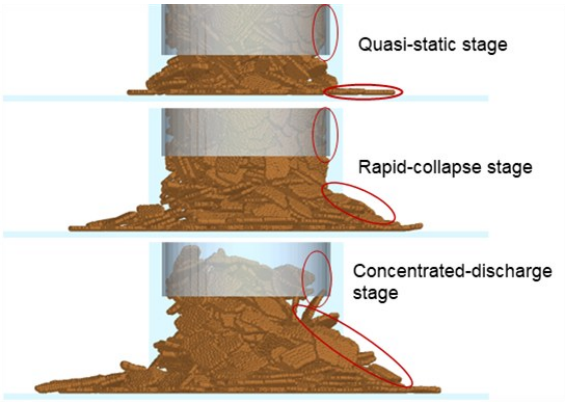


Fig. 15. The angle of repose generation phase in the cylinder lifting method

Optimization and validation of the angle of repose parameters

Contact parameters were optimized using the numerical optimization function in Design-Expert, with the experimentally measured mean angle of repose of 21.08° as the target. The objective function and constraints are given in Eq. 8.

$$\begin{cases} 0.217 \le X_3 \le 0.284 \\ 0.362 \le X_5 \le 0.455 \\ 0.166 \le X_6 \le 0.196 \\ \text{Angle of respose} = 21.08° \end{cases} \quad (8)$$

The optimization yielded 100 solutions satisfying the constraints. Parameter sets with high desirability were selected for validation through angle of repose simulations, and the optimal combination was identified by comparing the relative errors between the simulated and experimental angles of repose. The selected coefficients were 0.217 for static friction between walnut cake flakes X_3, 0.377 for restitution between walnut cake flakes X_5, and 0.166 for static friction between walnut cake flakes and steel X_6. Three simulations yielded a mean angle of repose of 21.43°, corresponding to a relative error of 1.66% compared with the experimental mean. The comparison in Fig. 16 shows that the optimized parameters reproduced both the pile morphology and the angle of repose observed experimentally, supporting their reliability for simulating walnut cake flakes piling behavior.



Fig. 16. Comparison of physical experiment and numerical simulation results for the angle of repose of walnut cake flakes

Meta-particle Modelling and Parameter Calibration of Bonded Particle Model for Walnut Cake Flakes

Bonded particle model

The Bonding V2 model, whose mechanism diagram is shown in Fig. 17, is a parallel-bond model proposed by Potyondy and Cundall and developed from the Hertz-Mindlin contact model to simulate the deformation and fracture of bonds between particles (Xu *et al*. 2023). In this model, the bonds generated between sub-particles constitute the force chains of the material, and the force-chain network formed by these bonds reflects the overall mechanical behavior of the material: while the bonds are intact, the load on the material is borne by the bonds, whereas after the bonds break, the load is borne independently by the particles. EDEM allows the bond formation time to be specified. A permanent bond forms between two particles when their center-to-center distance is less than the sum of their contact radii during the specified bond formation window. Once formed, the bond persists until failure and cannot regenerate after breaking. The incremental forces and moments acting on each bond at each time step are calculated using Eqs. 9 through 12, and bond failure is evaluated using the criteria in Eqs. 13 and 14 (Wang *et al*. 2024),

$$\delta F_{\mathrm{n}} = -v_{\mathrm{n}} S_{\mathrm{n}} A \delta t \tag{9}$$

$$\delta F_{\mathrm{t}} = -v_{\mathrm{t}} S_{\mathrm{t}} A \delta t \tag{10}$$

$$\delta M_{\mathrm{n}} = -\omega_{\mathrm{n}} S_{\mathrm{t}} J \delta t \tag{11}$$

$$\delta M_{\mathrm{t}} = \frac{-\omega_{\mathrm{t}} S_{\mathrm{n}} J \delta t}{2} \tag{12}$$

where F_{n} and F_{t} are the normal and Shear bond forces, respectively (N); M_{n} and M_{t} are the bond moments about the normal and Shear directions, respectively (N·m); δ denotes the increment in the corresponding quantity over one time step; v_{n} and v_{t} are the normal and

Shear velocities (m/s); ω_n and ω_t are the corresponding angular velocities (rad/s); S_n and S_t are the normal and Shear stiffnesses per unit area, respectively (N/m^3); A is the bond cross-sectional area (m^2); J is the polar second moment of area of the bond cross-section (m^4); and δ_t is the time step (s). The model can reproduce material deformation and failure and has been widely used in machinery applications in mining, agriculture, and chemical processing.

$$\sigma_{\max} < \frac{-F_n}{A} + \frac{2M_t}{J} R_B \tag{13}$$

$$\tau_{\max} < \frac{-F_t}{A} + \frac{M_n}{J} R_B \tag{14}$$

In these equations, $\sigma_{\max}$ and $\tau_{\max}$ are the normal and shear strengths of the bond, respectively (Pa), corresponding to the critical stress thresholds for bond failure. R_c denotes the bond cross-sectional radius (m), which is distinct from the particle contact radius specified in EDEM.

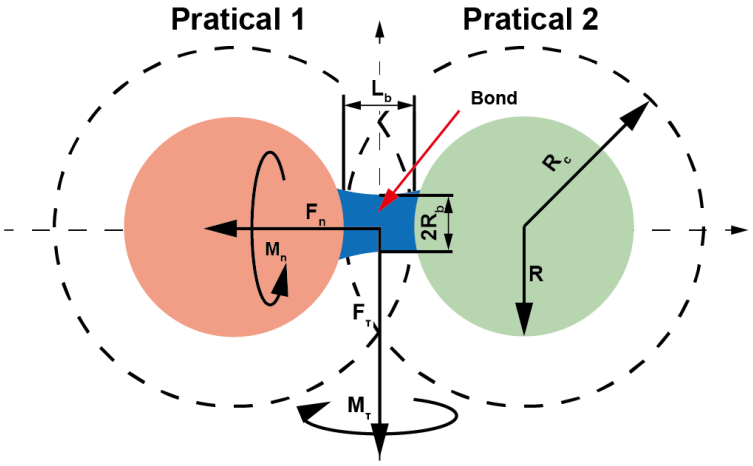


Fig. 17. Schematic diagram of the Bonding V2 model

Development of a bonded discrete element model for walnut cake flakes

The walnut cake flakes DEM model developed for contact parameter calibration contains overlapping sub-particles and too few particle layers, making it unsuitable for use with the parallel-bond model (PBM). The model therefore needs to be reconstructed for use with Bonding V2 by reducing the physical radius of the sub-particles and eliminating particle overlap. The reconstructed meta-particle model should contain more than three particle layers through its thickness to avoid numerical non-convergence and inaccurate force transmission through the force-chain network.

Meta-particles for the Bonding V2 model can be constructed using either the particle bed deposition method or the coordinate calculation method (Li *et al*. 2022; Jia *et al*. 2025). In the particle bed deposition method, a container is created in EDEM to accommodate a particle bed that fully encompasses the target meta-particle geometry. Once the particle bed has stabilized, the container is removed, and the particles within the target geometry are retained and their coordinates extracted. This method is straightforward to implement, but its limited packing uniformity makes it difficult to ensure the required number of particle layers through the thickness of thin, flake-like specimens. The coordinate calculation method uses tools such as MATLAB and ICEM to process the geometry of a 3D-scanned model and directly generate coordinates for regularly arranged

sub-particles. Although the workflow is more complex, it provides control over sub-particle arrangement and uniform packing, facilitating the construction of bond networks with specific topologies.

A walnut cake flakes meta-particle model incorporating a truss-like force-chain structure was developed using the coordinate calculation method. First, the geometry of an intact walnut cake flake specimen was captured using a handheld 3D scanner and exported as an STL model. The model was imported into MATLAB using the stlread function. A Cartesian coordinate system was established, and the model extents along the x, y, and z axes were determined to construct a rectangular bounding box enclosing the entire specimen. Candidate points were then generated using the mesh grid function. Taking r as the reference radius for coordinating generation, sub-particles were arranged in alternating staggered layers. Odd-numbered layers followed a square grid with a center-to-center spacing of 2r in both the x and y directions. Even-numbered layers were offset by r in both directions, placing each sub-particle directly above the center of the gap between four sub-particles in the layer below. The vertical spacing between adjacent layers was 1.75r. This arrangement increased the number of particle layers through the thickness of the flake-like specimen and enabled interparticle bonds to form a truss-like structure with inclined load-bearing connections, improving the stability of force transmission. Finally, candidate points within the STL geometry were identified using point-in-solid tests and retained as sub-particle center coordinates. To avoid particle overlapping and the resulting abrupt separation of the bonded assembly, the reference radius used for coordinate generation was set to 0.55 mm, whereas the physical radius of the sub-particles in EDEM was set to 0.5 mm. As shown in Figs. 18 and 19, the resulting DEM model closely reproduced the morphology of the walnut cake flake specimen. Within the interior of the model, each sub-particle formed four in-plane force-chain connections with its nearest neighbors and eight inclined connections with four neighbors in each of the adjacent layers. This connectivity produced a truss-like force-chain structure with greater stability under loading.

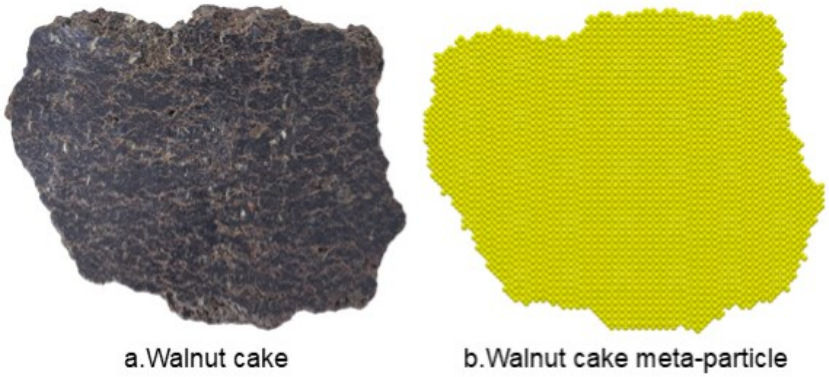


Fig. 18. Discrete element model of walnut cake flake

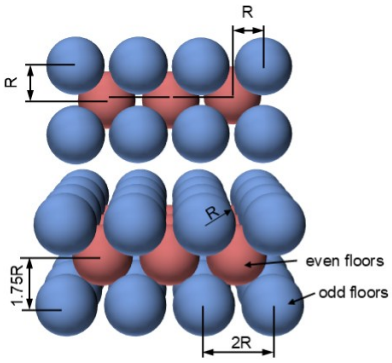


Fig. 19. Schematic of the meta particle model for walnut cake flake

Simulation setup of uniaxial compression test

Compression platens with a diameter of 100 mm, matching those used in the physical tests, were modeled in SolidWorks, exported in STL format, and imported into EDEM. The upper and lower platens were aligned coaxially with their loading surfaces facing each other. A single walnut cake flakes meta-particle was generated between the platens using a particle factory. Once the meta-particle had come to rest relative to the lower platen, the lower platen was held stationary while the upper platen moved vertically downward at a constant speed of 0.0833 mm/s. The simulation was stopped when the walnut cake flakes fractured, and the force curve for the upper platen was exported from the post-processing interface.

Steepest ascent test for the bonded parameters

Because the Bonding V2 parameters cannot readily be calculated directly from physical test measurements, their ranges for walnut cake flakes were established with reference to studies of hard, brittle agricultural materials, including brown rice (Shi *et al*. 2023), corn ears (Han *et al*. 2026), soybeans (Gou *et al*. 2026), and wheat (Wang *et al*. 2023), together with the official EDEM documentation. The parameter settings are listed in Table 8. The particle contact radius was set to 1.2 times the physical radius, and the Bonded Disk Scale was fixed at 1.2. The simulated F_f and the D_f at the same instant were used as responses. For each physical test, the maximum force and its corresponding displacement were extracted from the raw data and taken as the F_f and D_f, respectively. A complete experimental force-displacement curve was selected as the calibration reference, primarily on the basis of its F_f being close to the median, with D_f used as a secondary criterion to exclude markedly atypical results. This selection retained an actual measured curve for direct comparison with the simulation. The selected curve had a F_f of 48.73 N and a corresponding D_f of 2.032 mm, which were used as the calibration targets. The steepest ascent design and results are presented in Table 9.

Table 8. Bonding V2 Model Parameter Settings

Symbol	Parameters	Level	
		Low (-1)	High (1)
X_{b1}	Normal Stiffness per unit area (N/m^3)	3×10^{11}	1.1×10^{12}
X_{b2}	Shear Stiffness per unit area (N/m^3)	5×10^{9}	1.3×10^{10}
X_{b3}	Normal Strength/Pa	1×10^{6}	5×10^{6}
X_{b4}	Shear Strength/Pa	3×10^{5}	1.5×10^{6}

Table 9. Design and Results of the Steepest Ascent Test for Bonded Parameters

No.	X_{b1}	X_{b2}	X_{b3}	X_{b4}	F_f	Relative Error of F_f (%)	D_f
1	3×10^{11}	5×10^{9}	1×10^{6}	3×10^{5}	14.74	69.75	1.2435
2	5×10^{11}	7×10^{9}	2×10^{6}	6×10^{5}	35.87	26.39	1.4484
3	7×10^{11}	9×10^{9}	3×10^{6}	9×10^{5}	64.43	32.22	1.4346
4	9×10^{11}	1.1×10^{10}	4×10^{6}	1.2×10^{6}	71.11	45.93	1.6377
5	1.1×10^{12}	1.3×10^{10}	5×10^{6}	1.5×10^{6}	79.68	63.50	1.6276

Box-Behnken experiment of bonded parameters

In the steepest ascent test, Run 2 yielded the lowest relative error in F_f of 26.4%, with a corresponding relative error in D_f of 28.7%. Its parameter settings were therefore selected as the center levels for a Box-Behnken design, with those in Runs 1 and 3 defining the low and high levels, respectively. The design was used to investigate the relationship between the bonding parameters and the compressive fracture behavior of walnut cake flakes. A total of 29 simulation runs were conducted, with F_f and D_f as the responses. Each run was performed three times, and the mean values of both responses were used for analysis. The design and results are presented in Table 10.

Multiple regression analysis was performed to establish quadratic regression equations relating the F_f and D_f of walnut cake flakes to the Bonding V2 parameters, as expressed in Eqs. 15 and 16, respectively.

$$Y = 35.50 - 1.86X_{b1} + 0.8987X_{b2} + 18.47X_{b3} + 0.0571X_{b4} - 0.4287X_{b1}X_{b2} - 3.02X_{b1}X_{b3} - 0.0938X_{b1}X_{b4} + 0.9568X_{b2}X_{b3} + 0.1370X_{b3}X_{b4} + 1.39X_{b1}^2 - 0.3341X_{b2}^2 + 1.02X_{b3}^2 - 0.0898X_{b4}^2 \quad (15)$$

$$Y = 1.44 - 0.7062X_{b1} + 0.0315X_{b2} + 0.7651X_{b3} + 0.0029X_{b4} - 0.0337X_{b1}X_{b2} - 0.4323X_{b1}X_{b3} - 0.0050X_{b1}X_{b4} + 0.0342X_{b2}X_{b3} + 0.0054X_{b3}X_{b4} + 0.3173X_{b1}^2 - 0.0167X_{b2}^2 + 0.0337X_{b3}^2 - 0.0038X_{b4}^2 \quad (16)$$

Since the $X_{b2}X_{b4}$ term had an F value of 0, a P value of 1, and a regression coefficient of 0, it was removed by backward elimination. The ANOVA results of the adjusted regression models for F_f and D_f are presented in Tables 11 and 12, respectively. The P values of both models were below 0.05, indicating that both models were highly significant. For F_f, X_{b1}, X_{b3}, and their interaction, $X_{b1}X_{b3}$, had highly significant effects, whereas all remaining terms were not significant. The lack of fit was not significant, indicating a good fit of the model. The model had an R^2 of 0.9897, an adjusted R^2 of 0.9808, and an adequate precision of 36.7402. For D_f, X_{b1}, X_{b3}, $X_{b1}X_{b3}$, and X_{b1}^2 had highly significant effects, whereas all remaining terms were not significant. The lack of fit was also not significant. The corresponding R^2, adjusted R^2, and adequate precision were 0.9868, 0.9754, and 38.1085, respectively. These results indicated that both models provided good fits to the simulation data.

Table 10. Box-Behnken Experimental Design and Results of Bonded Parameters

No.	X_{b1}	X_{b2}	X_{b3}	X_{b4}	F_f (N)	D_f (mm)
1	7×10^{11}	7×10^{9}	2×10^{6}	3×10^{5}	35.3830	1.06291
2	5×10^{11}	7×10^{9}	3×10^{6}	3×10^{5}	53.2821	2.13081
3	5×10^{11}	9×10^{9}	1×10^{6}	6×10^{5}	18.6443	0.77469
4	5×10^{11}	9×10^{9}	3×10^{6}	6×10^{5}	55.6785	2.21411
5	5×10^{11}	7×10^{9}	1×10^{6}	3×10^{5}	18.4149	0.76969
6	5×10^{11}	5×10^{9}	2×10^{6}	3×10^{5}	35.4475	1.43942
7	3×10^{11}	7×10^{9}	2×10^{6}	3×10^{5}	37.6448	2.43069
8	7×10^{11}	5×10^{9}	2×10^{6}	6×10^{5}	34.3837	1.03958
9	3×10^{11}	7×10^{9}	1×10^{6}	6×10^{5}	18.6451	1.21785
10	5×10^{11}	9×10^{9}	2×10^{6}	3×10^{5}	36.0716	1.44775
11	5×10^{11}	7×10^{9}	2×10^{6}	6×10^{5}	35.8436	1.34895
12	5×10^{11}	7×10^{9}	2×10^{6}	6×10^{5}	36.2009	1.45275
13	5×10^{11}	5×10^{9}	1×10^{6}	6×10^{5}	18.0888	0.76136
14	7×10^{11}	7×10^{9}	1×10^{6}	6×10^{5}	17.9908	0.56477
15	5×10^{11}	7×10^{9}	2×10^{6}	6×10^{5}	35.8738	1.44775
16	3×10^{11}	9×10^{9}	2×10^{6}	6×10^{5}	38.7103	2.48067
17	5×10^{11}	7×10^{9}	3×10^{6}	9×10^{5}	53.8302	2.15247
18	7×10^{11}	7×10^{9}	3×10^{6}	6×10^{5}	52.4955	1.54771
19	3×10^{11}	7×10^{9}	2×10^{6}	9×10^{5}	37.9008	2.44735
20	3×10^{11}	5×10^{9}	2×10^{6}	6×10^{5}	35.5540	2.31407
21	7×10^{11}	7×10^{9}	2×10^{6}	9×10^{5}	35.2640	1.05958
22	5×10^{11}	7×10^{9}	1×10^{6}	9×10^{5}	18.4149	0.76969
23	5×10^{11}	7×10^{9}	2×10^{6}	6×10^{5}	34.0338	1.51365
24	5×10^{11}	5×10^{9}	2×10^{6}	9×10^{5}	35.4475	1.43942
25	7×10^{11}	9×10^{9}	2×10^{6}	6×10^{5}	35.8250	1.07124
26	5×10^{11}	7×10^{9}	2×10^{6}	6×10^{5}	35.5265	1.44775
27	5×10^{11}	9×10^{9}	2×10^{6}	9×10^{5}	36.0716	1.44775
28	3×10^{11}	7×10^{9}	3×10^{6}	6×10^{5}	65.2415	3.93009
29	5×10^{11}	5×10^{9}	3×10^{6}	6×10^{5}	51.2957	2.06417

Table 11. Analysis of ANOVA for Fracture Force

Parameter	Sum of squares	Freedom	Mean Square	*F* Values	*P* Values
Model	4206.51	13	323.58	110.88	< 0.0001**
X_{b1}	41.64	1	41.64	14.27	0.0018**
X_{b2}	9.69	1	9.69	3.32	0.0884
X_{b3}	4093.13	1	4093.13	1402.54	< 0.0001**
X_{b4}	0.0391	1	0.0391	0.0134	0.9094
$X_{b1}X_{b2}$	0.7353	1	0.7353	0.2520	0.6230
$X_{b1}X_{b3}$	36.55	1	36.55	12.52	0.0030*
$X_{b1}X_{b4}$	0.0352	1	0.0352	0.0120	0.9141
$X_{b2}X_{b3}$	3.66	1	3.66	1.25	0.2802
$X_{b3}X_{b4}$	0.0751	1	0.0751	0.0257	0.8747
X_{b1}^2	12.59	1	12.59	4.32	0.0554
X_{b2}^2	0.7242	1	0.7242	0.2482	0.6256
X_{b3}^2	6.70	1	6.70	2.30	0.1505
X_{b4}^2	0.0523	1	0.0523	0.0179	0.8952
Residual	43.78	15	2.92		
Lack of Fit	40.88	11	3.72	5.13	0.0641
Pure Error	2.90	4	0.7249		
Summation	4250.28	28			
R_2 = 0.9897; Adj R^2 = 0.9808; CV = 4.70%; Adeq Precision = 36.7402					

Table 12. Analysis of ANOVA for Fracture Displacement

Parameter	Sum of squares	Freedom	Mean Square	*F* Values	*P* Values
Model	14.49	13	1.11	86.52	< 0.0001**
X_{b1}	5.99	1	5.99	464.56	< 0.0001**
X_{b2}	0.0119	1	0.0119	0.9251	0.3514
X_{b3}	7.02	1	7.02	545.23	< 0.0001**
X_{b4}	0.0001	1	0.0001	0.0079	0.9303
$X_{b1}X_{b2}$	0.0046	1	0.0046	0.3534	0.5611
$X_{b1}X_{b3}$	0.7476	1	0.7476	58.03	< 0.0001**
$X_{b1}X_{b4}$	0.0001	1	0.0001	0.0078	0.9310
$X_{b2}X_{b3}$	0.0047	1	0.0047	0.3621	0.5563
$X_{b3}X_{b4}$	0.0001	1	0.0001	0.0091	0.9253
X_{b1}^2	0.6531	1	0.6531	50.69	< 0.0001**
X_{b2}^2	0.0018	1	0.0018	0.1407	0.7129
X_{b3}^2	0.0074	1	0.0074	0.5711	0.4615
X_{b4}^2	0.0001	1	0.0001	0.0073	0.9331
Residual	0.1933	15	0.0129		
Lack of Fit	0.1793	11	0.0163	4.67	0.0750
Pure Error	0.0140	4	0.0035		
Summation	14.68	28			
R^2 = 0.9868; Adj R^2 = 0.9754; CV = 7.19%; Adeq Precision = 38.1085					

As shown in Fig. 20, the response surface exhibits slight concavity. At a constant normal strength X_{b3}, the F_f of walnut cake flakes increases slightly and monotonically with increasing normal stiffness per unit area X_{b1}, indicating a relatively small influence of X_{b1} on F_f. At a fixed X_{b1}, however, F_f increases markedly with increasing X_{b3}, indicating a significant influence of normal strength. As shown in Fig. 21, the response surface exhibits pronounced concavity. At a constant X_{b3}, D_f initially increases slightly and then decreases as X_{b1} increases, indicating that normal stiffness per unit area has some influence on the displacement at fracture. At a fixed X_{b1}, D_f increases markedly with increasing X_{b3}, demonstrating the significant influence of normal strength on this response.

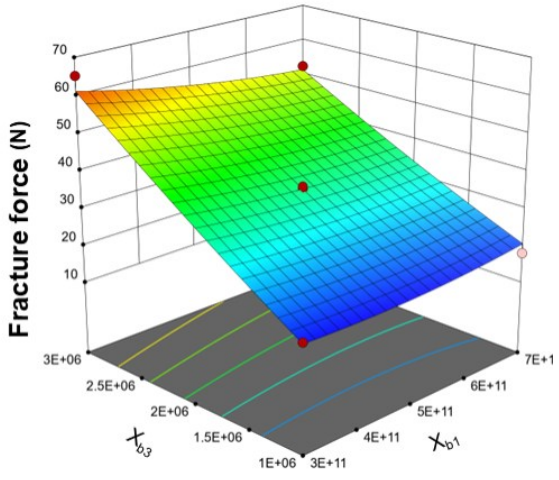


Fig. 20. Response surface for fracture force of item $X_{b1}X_{b3}$

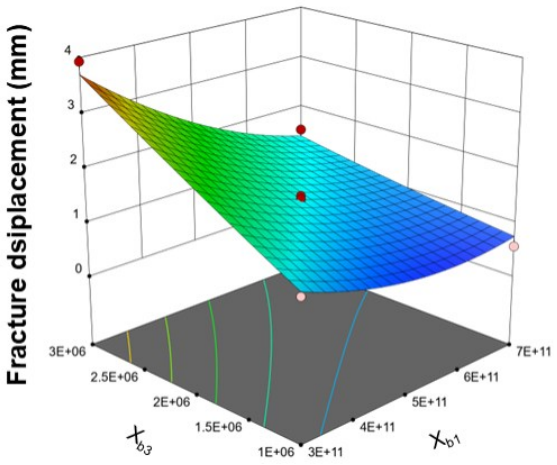


Fig. 21. Response surface for fracture displacement of item $X_{b1}X_{b3}$

The mechanisms of the Bonding V2 model, together with the response surface results, indicate that normal strength X_{b3} is the dominant factor governing bond fracture in the model. The discrete element model developed in this study employs a highly ordered meta-particle packing arrangement, resulting in a truss-like force-chain structure. During uniaxial compression of the arched walnut cake flake, load transmission through the force-chain network is dominated by normal compression of the bonds, with relatively weak shear effects. As compression progresses, however, vertical compression and lateral extension of the flake generate tensile stress along the tangent to the arch near the cross-section at the apex. In the local coordinate systems of the bonds, this stress is predominantly resolved into normal tensile stress, with a smaller shear component. Consequently, the tensile failure threshold of the bonds is primarily controlled by normal strength X_{b3}, whereas the response is less sensitive to shear strength X_{b4} under these loading conditions.

Normal stiffness per unit area X_{b1} is a secondary factor that determines the forces carried by the bonds at a given displacement and the overall stiffness of the specimen. As illustrated in the model, particles in even-numbered layers form bonds with particles within the same layer and, together with particles in the adjacent odd-numbered layers above and below, constitute rectangular prism cells. Each particle in an even-numbered layer occupies the center of a cell and forms eight diagonal bonded connections with the particles at its eight vertices. These diagonal force chains resolve the macroscopic shear load acting on the cross-section at the arch apex into axial forces normal to the cross-sections of the inclined bonds. Meanwhile, the intra-layer force chains perpendicular to the fracture plane also contribute to carrying the shear load on this cross-section through normal bond forces. Most of the shear load is thus transferred through axial bond forces, allowing normal stiffness to contribute substantially to the overall specimen stiffness. The effects of shear strength X_{b4} and shear stiffness per unit area X_{b2} are comparatively small because most of the load is already carried by the normal bond components, limiting the contributions of these shear parameters to fracture force and displacement.

Among the interaction terms, only $X_{b1}X_{b3}$ is significant. This interaction arises because the truss-like force-chain structure transfers load primarily through the normal bond components: normal stiffness governs the force-displacement relationship, whereas normal strength defines the limit of the bond's capacity to sustain normal forces and associated moments.

Uniaxial compression test validation

The bonding parameters were similarly optimized using the numerical optimization function in Design-Expert, with the uniaxial compression F_f (48.73 N) and the corresponding displacement at fracture (2.032 mm) of walnut cake flakes specified as target values. The objective function and constraints are given in Eq. 17.

$$\begin{cases} F_b = 48.73 \\ D_b = 2.032 \\ 3\mathrm{E}+11 \le X_{b1} \le 7\mathrm{E}+11 \\ 5\mathrm{E}+09 \le X_{b2} \le 9\mathrm{E}+09 \\ 1\mathrm{E}+06 \le X_{b3} \le 3\mathrm{E}+06 \\ 3\mathrm{E}+05 \le X_{b4} \le 9\mathrm{E}+05 \end{cases} \quad (17)$$

A total of 100 candidate parameter combinations were obtained through optimization. Uniaxial compression simulations were conducted for each combination, and the optimal set was selected by comparing the simulated fracture mode, F_f, and D_f with the physical test results. The selected parameters were a normal stiffness per unit area of 4.91 × 10^{11} N/m^3, a shear stiffness per unit area of 7.71 × 10^9 N/m^3, a normal strength of 2.66 × 10^6 Pa, and a shear strength of 7.04 × 10^5 Pa. The mean F_f and D_f from three simulation runs were 48.317 N and 1.964 mm, respectively, corresponding to relative errors of 0.85% and 3.35% compared with the experimental targets. Shear strength, however, showed very low sensitivity under the present uniaxial compression conditions.

Figure 22 compares the experimental and simulated force-displacement curves. The experimental curve exhibited fluctuations during compression, which can be attributed to the numerous small pores and pre-existing cracks within the walnut cake flakes. In contrast, the discrete element model, with its truss-like force-chain structure, produced a predominantly linear response before fracture, approaching that of an ideal brittle material. Figure 23 compares the experimental and simulated fracture morphologies. Both exhibited an opening-mode fracture at the cross-section near the arch apex, with crack propagation perpendicular to the principal tensile stress direction. In the physical test, the main crack deviated slightly from the geometric center, and pre-existing fissures promoted the development of wing cracks during propagation. By contrast, the meta-particle model was constructed from calculated node coordinates, yielding a more regular particle arrangement and a fracture path more closely aligned with the geometric center.

These results demonstrate that the optimized parameter set can effectively reproduce the principal mechanical responses and fracture characteristics of walnut cake flakes under uniaxial compression, supporting its reliability for simulating the loading conditions investigated in this study.

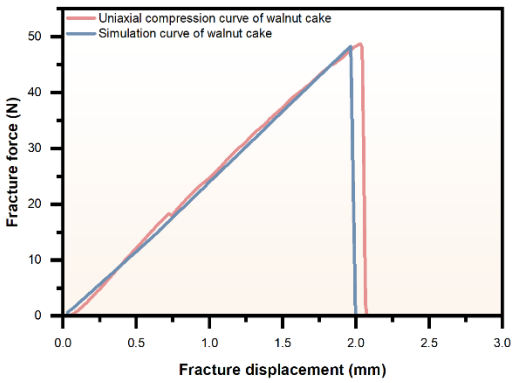


Fig. 22. Comparison of force-displacement curves between numerical simulation and physical test for walnut cake flakes

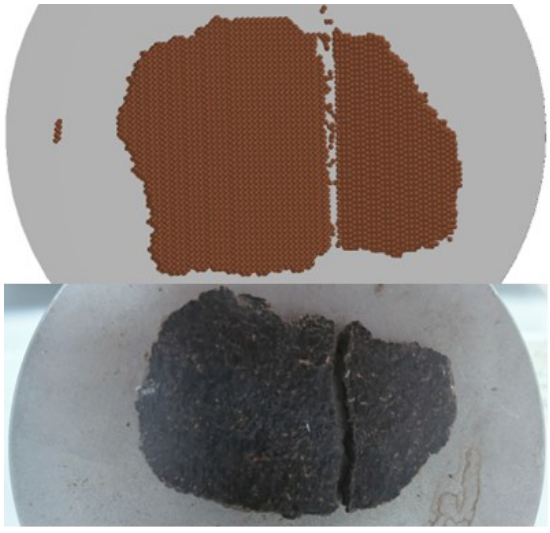


Fig. 23. Comparison of crack morphologies between numerical simulation and physical test for walnut cake flakes

CONCLUSIONS

1. The morphological characteristics of walnut cake flakes were captured by 3D scanning to construct three-dimensional models, while the particle size distribution was determined directly by sieve analysis (Table 1). For contact parameter calibration, discrete element models of walnut cake flakes particles measuring 15 to 20 mm were generated using the automatic filling method in EDEM. For Bonding V2 parameter calibration, a meta-particle modeling method incorporating a truss-like force-chain structure was developed using node coordinates calculated in MATLAB. The method successfully reproduced the principal fracture metrics and morphology under uniaxial compression, demonstrating its feasibility and providing a viable approach to constructing meta-particle models of thin, flake-like agricultural materials.
2. The basic physical properties of walnut cake flakes, including density, elastic modulus, and Poisson's ratio, were determined experimentally. The ranges of contact parameters for walnut cake flakes-walnut cake flakes and walnut cake flakes-steel interactions were measured using the roller-inclined plane method. The angle of repose was measured using the cylinder lifting method, yielding a value of 21.08° by averaging the angles on both sides of the pile. A Box-Behnken design was used to establish a quadratic regression model relating the significant factors to the angle of repose. Using the measured angle of repose as the optimization target, the optimal parameter combination was determined as follows: coefficient of static friction between walnut cake flakes of 0.217, coefficient of restitution between walnut cake flakes of 0.377, and coefficient of static friction of walnut cake flakes-stainless steel of 0.166. Three simulation runs yielded a mean angle of repose of 21.43°, corresponding to a relative error of 1.66% compared with the experimental value.
3. The compressive mechanical properties of walnut cake flakes were determined through uniaxial compression tests. A representative experimental curve was selected primarily on the basis of its F_f being close to the median, with D_f serving as a secondary selection criterion. Its F_f of 48.73 N and corresponding displacement of 2.032 mm were used as calibration targets. The ratio of contact radius to physical radius and the Bonded Disk Scale were both fixed at 1.2. Response surface analysis was performed with normal stiffness per unit area, shear stiffness per unit area, normal strength, and shear strength as factors, and F_f and D_f as responses. The optimal parameter combination comprised a normal stiffness per unit area of 4.91×10^{11} N/m^3, a shear stiffness per unit area of 7.71×10^{9} N/m^3, a normal strength of 2.66×10^{6} Pa, and a shear strength of 7.04×10^{5} Pa. Verification simulations yielded relative errors of 0.85% in F_f and 3.35% in D_f. The simulated fracture behavior was consistent with the experimental observations, supporting the reliability of the developed discrete element model under the investigated conditions. The model provides a theoretical basis for further studies of walnut cake flakes material properties and its resource utilization.

ACKNOWLEDGMENTS

This research was supported by the 2026 Innovation Development and Service Program of the Department of Agriculture and Rural Affairs of the Xinjiang Uygur Autonomous Region through the project "Development of Key Technologies for the

Utilization of Walnut Deep-Processing by-products in Aquaculture Feed" (Project No. NTFW-2026-14).

Conflict of Interest

The authors declare that there are no personal interests or relationships that could potentially be affected by the publication of this manuscript.

Use of Generative AI

Generative-AI tool was employed for English translation and linguistic polishing of the manuscript text. All experimental data, simulation results, figures, graphs and diagrams in this work were independently produced by the authors without generative-AI assistance.

REFERENCES CITED

Ai, X., Yi, J., Pei, Z., Zhou, W., and Feng, D. (2024). "Advances in discrete element modeling of asphalt mixture: A literature review," *Archives of Computational Methods in Engineering* 31, 4003-4029. https://doi.org/10.1007/s11831-024-10104-8

Cao, S., Xiang, F., Li, S., Ma, X., Hu, H., Guo, Q., Jiao, B., Agyei, D., Wang, Q., and Shi, A. (2024). "Characteristics of walnut oil and the residual cake prepared using various pretreatment and extraction methods," *LWT* 206, article 116596. https://doi.org/10.1016/j.lwt.2024.116596

Gou, F., Ni, Y., Qian, Z., Yang, T., Jin, C., Wang, J., and Li, M. (2026). "A study on the calibration method of bonding parameters for soybean threshing materials based on GA-BP model and whale optimization algorithm," *Powder Technology* 469(1), article 121711. https://doi.org/10.1016/j.powtec.2025.121711

Han, D., Mo, T., Wang, Y., Tang, C., Chen, L., and Xu, L. (2026). "Measurement and calibration of bonding parameters for a multi-scale DEM model of corn ears: Experiment and simulation alignment," *Advanced Powder Technology* 37(2), article 105175. https://doi.org/10.1016/j.apt.2026.105175

Jia, X., Zheng, X., Chen, L., Liu, C., Song, J., Zhu, C., Xu, J., and Hao, S. (2025). "Discrete element flexible modeling and experimental verification of rice blanket seedling root blanket," *Computers and Electronics in Agriculture* 233, article 110155. https://doi.org/10.1016/j.compag.2025.110155

Lei, J., Ren, D., Liu, Z., Wang, S., Lei, D., Luo, J., and Lei, M. (2023). "Discrete element contact parameters measurement and calibration of sugarcane leaves based on RSM-PSO," *BioResources* 18(3), 4994-5012. https://doi.org/10.15376/biores.18.3.4994-5012

Li, D., Chang, Z., Wang, D., Li, X., Zhang, J., Yan, H., Zuo, B., and Hou, J. (2026). "Development of a DEM-based flexible plant model for mature peanut plants," *Agriculture* 16(13), article 1390. https://doi.org/10.3390/agriculture16131390

Li, J., Lu, Y., Peng, X., Jiang, P., Zhang, B., Zhang, L., Meng, H., Kan, Z., and Wang, X. (2022). "Discrete element method for simulation and calibration of cotton stalk contact parameters," *BioResources* 18(1), 400-416. https://doi.org/10.15376/biores.18.1.400-416

Li, J., Zhang, W., Li, D., and Yu, Y. (2025). "Parameter calibration and testing for discrete element simulation of walnut kernels," *Computational Particle Mechanics*

12(6), 5183-5196. https://doi.org/10.1007/s40571-025-00995-0

Li, X., Du, Y., Liu, L., Zhang, Y., and Guo, D. (2022). "Parameter calibration of corncob based on DEM," *Advanced Powder Technology* 33(8), article 103699. https://doi.org/10.1016/j.apt.2022.103699

Li, X., Xu, Y., Zhou, J., Wang, H., Xu, X., and Zuo, J. (2026). "Discrete elemental parameter calibration and experiments for mechanically harvested dried safflower filaments," *Transactions of the Chinese Society of Agricultural Engineering* 42(4), 150-160. https://doi.org/10.11975/j.issn.1002-6819.202505137

Li, Y., Wang, W., Qiao, H., Zhao, Y., and Tian, X. (2024). "Discrete element parameter calibration during cottonseed crushing process," *BioResources* 19(4), 8694-8711. https://doi.org/10.15376/biores.19.4.8694-8711

Liu, M., Wang, J., You, Z., Wu, Y., Wang, N., and Xie, H. (2024). "Experimental calibration of parameters of discrete element model for ginkgo nut," *BioResources* 19(4), 8154-8172. https://doi.org/10.15376/biores.19.4.8154-8172

Ma, X., Huang, C., Zheng, C., Wang, W., Ying, H., and Liu, C. (2024). "Effect of oil extraction methods on walnut oil quality characteristics and the functional properties of walnut protein isolate," *Food Chemistry* 438, article 138052. https://doi.org/10.1016/j.foodchem.2023.138052

Ning, T., Zhang, Y., and Wang, X. (2026). "Application of numerical simulation technology in the biomass densification and molding field: A review," *BioResources* 21(1), 2649-2668. https://doi.org/10.15376/biores.21.1.2649

Ojeda-Amador, R. M., Salvador, M. D., Gómez-Alonso, S., and Fregapane, G. (2018). "Characterization of virgin walnut oils and their residual cakes produced from different varieties," *Food Research International* 108, 396-404. https://doi.org/10.1016/j.foodres.2018.03.066

Ren, J., Wu, T., Mo, W., Li, K., Hu, P., Xu, F., and Liu, Q. (2022). "Discrete element simulation modeling method and parameters calibration of sugarcane leaves," *Agronomy* 12(8), article 1796. https://doi.org/10.3390/agronomy12081796

Shi, Y., Jiang, Y., Wang, X., Thuy, N. T. D., and Yu, H. (2023). "A mechanical model of single wheat straw with failure characteristics based on discrete element method," *Biosystems Engineering* 230, 1-15. https://doi.org/10.1016/j.biosystemseng.2023.03.017

Shi, Z., Liu, X., Zhang, Y., Zhou, J., Li, H., and Duan, F. (2023). "Bond parameter calibration and crushing process analysis of brown rice kernels," *Processes* 11(10), article 2992. https://doi.org/10.3390/pr11102992

Spréa, R. M., Rodrigues, D. B., Pires, T. C. S., Calhelha, R. C., Brassesco, M. E., Pintado, M., Santoyo, S., Arranz, E., Prieto, M. A., Barros, L., and Amaral, J. S. (2026). "Comprehensive characterization of walnut oil processing by-products: Biochemical composition, bioactive properties, and polyphenol in vitro bioaccessibility and bioavailability," *Food Chemistry* 525, article 149641. https://doi.org/10.1016/j.foodchem.2026.149641

Sun, K., Yu, J., Zhao, J., Liang, L., Wang, Y., and Yu, Y. (2023). "A DEM-based general modeling method and experimental verification for wheat plants in the mature period," *Computers and Electronics in Agriculture* 214, article 108283. https://doi.org/10.1016/j.compag.2023.108283

Teh, X. W., Chang, Y. P., and Lee, K. C. (2021). "Upgrading the fermentability and prebiotic potential of palm decanter cake through fibre-degrading enzymatic treatments," *IOP Conference Series: Earth and Environmental Science* 945, article

012076. https://doi.org/10.1088/1755-1315/945/1/012076
Wang, X., Wu, W., and Jia, H. (2023). "Calibration of discrete element parameters for simulating wheat crushing," *Food Science & Nutrition* 11(12), 7751-7764. https://doi.org/10.1002/fsn3.3693
Wang, Y., Lin, G., Liu, X., Zhao, L., Jia, B., Wang, Y., and He, J. (2024). "Research on coal rock parameter calibration based on discrete element method," *Scientific Reports* 14, article 26507. https://doi.org/10.1038/s41598-024-77538-9
Xu, C., Xu, F., Tang, H., and Wang, J. (2023). "Determination of characteristics and establishment of discrete element model for whole rice plant," *Agronomy* 13(8), article 2098. https://doi.org/10.3390/agronomy13082098
Yang, L., Yu, Y., Wang, C., Hu, L., Ma, Y., Zi, F., Ma, R., Huo, Q., Song, Y., Sun, Z., Lin, X., Ren, D., and Chen, S. (2025). "Analysis and evaluation of the muscle quality of high-salinity aquaculture fish in Xinjiang, China," *Journal of Food Composition and Analysis* 144, article 107750. https://doi.org/10.1016/j.jfca.2025.107750
Zhang, J., Xie, J., Du, Y., Li, Y., Yue, Y., and Cao, S. (2024). "Discrete element modeling and experimental study of biomechanical properties of cotton stalks in machine-harvested film-stalk mixtures," *Scientific Reports* 14, article 12933. https://doi.org/10.1038/s41598-024-62390-8
Zhang, W., Cao, Q., Li, Z., and Jiang, P. (2026). "Characterization of physical, mechanical, and shear properties of cabbage stubble and calibration of its discrete element method parameters," *Agriculture* 16(15), article 1600. https://doi.org/10.3390/agriculture16151600
Zhang, W., Zhou, J., Xu, Y., Chen, X., Gao, Y., and Qiu, Y. (2026). "Calibration and experimental validation of discrete element model parameters for cotton stalks and cotton residues mixture," *Agriculture* 16, article 1492. https://doi.org/10.3390/agriculture16141492
Zhang, Z., Bao, G., Yuan, Y., Lv, Z., Chen, X., Tao, C., Li, J., and Yang, W. (2025). "The calibration and validation of discrete element model contact parameters for the soil-white radish root-petiole-clamping device system during the harvesting period," *Computers and Electronics in Agriculture* 239, article 111069. https://doi.org/10.1016/j.compag.2025.111069
Zhao, W., Chen, M., Xie, J., Cao, S., Wu, A., and Wang, Z. (2023). "Discrete element modeling and physical experiment research on the biomechanical properties of cotton stalk," *Computers and Electronics in Agriculture* 204, article 107502. https://doi.org/10.1016/j.compag.2022.107502

Article submitted: September 8, 2026; Peer review completed: October 11, 2026; Revised version received: October 21, 2026; Accepted: November 1, 2026; Published: November 18, 2026.
DOI: 10.15376/biores.22.1.558-584